ISTITUTO NAZIONALE DI RICERCA METROLOGICA
Repository Istituzionale

Simplified modeling of implanted medical devices with metallic filamentary closed loops exposed to low or medium frequency magnetic fields

(Article begins on next page)

21 May 2024

Simplified modeling of implanted medical devices with metallic filamentary closed loops exposed to low or medium frequency magnetic fields

Oriano Bottauscio*, Alessandro Arduino, Mario Chiampi, Luca Zilberti

Istituto Nazionale di Ricerca Metrologica (INRiM), Strada Delle Cacce 91, 10135 Torino, Italy

ABSTRACT

Background and objectives: Electric currents are induced in implanted medical devices with metallic filamentary closed loops (e.g., fixation grids, stents) when exposed to time varying magnetic fields, as those generated during certain diagnostic and therapeutic biomedical treatments. A simplified methodology to efficiently compute these currents, to estimate the altered electromagnetic field distribution in the biological tissues and to assess the consequent biological effects is proposed for low or medium frequency fields.
Methods: The proposed methodology is based on decoupling the handling of the filamentary wire and the anatomical body. To do this, a circuital solution is adopted to study the metallic filamentary implant and this solution is inserted in the electromagnetic field solution involving the biological tissues. The Joule losses computed in the implant are then used as a forcing term for the thermal problem defined by the bioheat Pennes' equation. The methodology is validated against a model problem, where a reference solution is available.
Results: The proposed simplified methodology is proved to be in good agreement with solutions provided by alternative approaches. In particular, errors in the amplitude of the currents induced in the wires result to be always lower than 3%. After the validation, the methodology is applied to check the interactions between the magnetic field generated by different biomedical devices and a skull grid, which represents a complex filamentary wire implant.
Conclusions: The proposed simplified methodology, suitable to be applied to closed loop wires in the low to intermediate frequency range, is found to be sufficiently accurate and easy to apply in realistic exposure scenarios. This modeling tool allows analyzing different types of small implants, from coronary and biliary duct stents to orthopedic grids, under a variety of exposure scenarios.

© 2022 The Authors. Published by Elsevier B.V. This is an open access article under the CC BY-NC-ND license (http://creativecommons.org/licenses/by-nc-nd/4.0/)

1. Introduction

In silico models are a powerful tool largely adopted for analyzing the interaction between electromagnetic fields (EMFs) and human beings, with the main scope of evaluating the safety of technologies and optimizing their effectiveness [1]. In recent years, considerable efforts have been devoted to the study of the interactions with implanted medical devices, largely spread among the population [2]. Metallic objects within the human body can enhance the power deposition, producing temperature increases in native tissues, or modify the induced electric field, which may cause peripheral nerve stimulation [3–6]. Among the possible exposure scenarios, a significant number is due to biomedical technologies that use EMFs for diagnostic or therapeutic purposes, such as Magnetic Resonance Imaging (MRI) [7], Magnetic Hyperthermia (MH) [8] or Transcranial Magnetic Stimulation (TMS) [9].

A large literature discusses the exposure of patients bearing implants during MRI scanning [10]. Particular attention has been paid to active implantable medical devices (AIMD) (e.g., cardiac defibrillators [10] and Deep Brain Stimulators, DBS [11]), but also passive implants (e.g., fixation grids, stents) were studied in recent years [12–15]. *In silico* models were also applied to biomedical technologies under development, to identify possible exclusion criteria for patients carrying implants (see for example [16], related to MH treatments).

* Corresponding author.
   E-mail address: o.bottauscio@inrim.it (O. Bottauscio).

Powerful computational methodologies, often supported by commercial software, are available for investigating the interaction between EMFs and anatomical models in presence of implants. Nonetheless, some analyses remain a challenge due to specific geometrical or functional characteristics of the electromagnetic problem [17], like the case of implanted devices including metallic filaments.

Metallic wires connect the pulse generator to the local electrodes in AIMD, but structures composed of thin wires can be found also in passive implants, such as the metallic stents adopted to enlarge vessels or ducts [18], or the metallic grids used in orthopedics to fix bone fractures [19]. The extremely small diameter of the wires (down to 0.1 mm or lower) makes the adoption of voxelized anatomical models (whose elements have typical size of 1 mm) not straightforward. Indeed, a voxel size suitable to reproduce the wire geometry would increase the computational burden of the electromagnetic simulations significantly. Non-structured meshes could be adopted in this case, as, for example, in the studies of the local Specific Absorption Rate (SAR) deposition caused by DBS electrodes [20] or cardiac leads [21] due to MRI radiofrequency fields. However, in the presence of implants with a complex shape, the pre-processing phase required to discretize the anatomical models could be critical and the mesh quality remains an issue.

In order to preserve a voxel-based discretization, the Huygens approach [22] is often adopted in literature, decomposing the problem in two subsequent simulations. The first one is performed in the entire anatomical model without the metallic wires using a rough mesh and provides the boundary conditions to the successive simulation, which includes only a portion of the original domain around the wire, discretized with a considerably finer mesh. For example, in [23] a mesh size down to 0.05 mm was adopted to handle helical structures in DBS. The reciprocity theorem and the Huygens principle were also adopted in [24,25] to alleviate potential errors in evaluating the electric field at the electrode tip.

Advanced algorithms based on adaptive meshing [26], multiscale approaches [27] or perturbation techniques [28] were also proposed in literature. All these models adopt the Perfect Electric Conductor (PEC) approximation to handle metal components exposed to radiofrequency (RF) EMFs [29,30], or its extension represented by surface impedance boundary conditions (SIBC) [31]. This assumption significantly reduces the discretization effort since the mesh does not have to fit the penetration depth δ of the radiation in the metal (e.g., $\delta \sim 50$ μm at 100 MHz for an electrical conductivity equal to 10^6 S/m), but does not hold at lower frequencies, where currents are induced deeply inside the wires.

An alternative to meshing the filamentary structure together with the anatomical model is to introduce a surrogate model for the device. At RF, a common approach to describe elongated wires uses a transfer function, which relates the tangential component of the incident electric field to the scattered electric field at its tip [32–34]. Extension to short wires was also proposed [35]. This method, which is implant-specific, allows coupling the experimental characterization of the implant with simulations [36].

The above-mentioned approaches are suitable for open wires. Anyway, some drawbacks arise at intermediate frequencies, especially in presence of closed loops with complex structures (e.g., grids composed of many wires), where the circulation of the current within the closed loops produces power dissipation and heats the surrounding tissues. Circuital approaches have been proposed to model the interaction of metallic wires with magnetic fields, but their application was limited to fields at 50 Hz [37,38].

This paper proposes a simplified methodology for the dosimetric analysis, at the intermediate frequencies, of anatomical models which include metallic filamentary closed loops. The simplified methodology is based on the combination of a circuit and a field analysis, where the metallic filamentary implant is described by 1D curves, which are included in the tissue as a separate structure without requiring constraints for the meshing. The system of curves is handled through an equivalent electrical network that interacts with the EMF computation. The approach relies on some preliminary assumptions, detailed in Sect. 2, which strictly define its applicability range. The output of the electromagnetic analysis is then used as the forcing term for Pennes' bioheat equation [39,40], which provides the time evolution of the temperature distribution within the biological tissues.

2. Numerical methodology

2.1. Electromagnetic field problem

The domain under analysis is a portion of the human body. It includes biological tissues (domain Ω), having electrical conductivity σ, and metallic wires (domain Γ), forming closed loops. The electric field is induced both in the tissues and in the metallic wires, producing currents.

The following assumptions are introduced:

a) The magnetic field generated by the currents induced in the tissues does not appreciably affect the magnetic field generated by the external sources.

b) The magnetic field generated by the currents induced in the metallic wires may be significant and perturb the magnetic field generated by the external sources.

c) The currents induced in the metallic wires are confined within the closed loops and are not drained towards the surrounding tissues. This assumption is motivated by the considerably higher conductivity of metal with respect to tissues and the small size of the implants with respect to the wavelength, but it makes the proposed method valid only in presence of entirely closed metallic wire loops and precludes its application to the case of open-wires where the return path of the currents involves the surrounding tissues.

d) The currents induced in the body are confined within the body itself.

e) The frequency is limited to values for which the effects of the field propagation within the body are negligible and the dielectric component of the induced currents can be disregarded with respect to the ohmic component.

The electromagnetic field problem at steady-state is solved in the frequency domain (angular frequency ω), where all field quantities are represented through the corresponding phasors. Thus, the transient evolution of the electromagnetic field is disregarded (as usual in electromagnetic dosimetry analysis, for periodic driving terms). The computation of thermal evolution is not affected by this assumption, because its characteristic time largely exceeds that of the electromagnetic phenomenon.

The electric field $\boldsymbol{E}$ is written as:

$$\boldsymbol{E}(\boldsymbol{r}) = \nabla\varphi(\boldsymbol{r}) - \mathrm{i}\omega\boldsymbol{A}(\boldsymbol{r}), \tag{1}$$

where $\boldsymbol{A}$ is the magnetic vector potential, φ is the electric scalar potential, $\boldsymbol{r}$ is the position, and i is the imaginary unit. Based on the assumptions introduced above, the magnetic vector potential $\boldsymbol{A}$ is the sum of two terms, $\boldsymbol{A} = \boldsymbol{A}_{\mathrm{s}} + \boldsymbol{A}_{\mathrm{r}}$, where $\boldsymbol{A}_{\mathrm{s}}$ is the source term (here assumed to be given by external coils) and $\boldsymbol{A}_{\mathrm{r}}$ is the reaction term due to the currents induced in the metallic wires embedded into the biological tissues. If the field source is a system of currents without magnetic materials, $\boldsymbol{A}_{\mathrm{s}}$ is written as

$$\boldsymbol{A}_{\mathrm{s}}(\boldsymbol{r}) = \mu_0 \int_{\Omega_{\mathrm{s}}} \psi(\boldsymbol{r} - \boldsymbol{r}_0)\, \boldsymbol{J}_{\mathrm{s}}(\boldsymbol{r}_0)\, d\boldsymbol{r}_0, \tag{2}$$

where Ω_s is the domain of the field sources, $\boldsymbol{J}_s$ is the current density imposed into the external coils, and $\psi(\boldsymbol{x}) = (4\pi|\boldsymbol{x}|)^{-1}$ is the Green function for the Laplace equation.

Similarly, the reaction term $\boldsymbol{A}_r$ is written as

$$\boldsymbol{A}_r(\boldsymbol{r}) = \mu_0 \int_\Gamma \psi(\boldsymbol{r} - \boldsymbol{r}_0)\,\boldsymbol{J}_w(\boldsymbol{r}_0)\,d\boldsymbol{r}_0, \tag{3}$$

where $\boldsymbol{J}_w$ is the unknown current density induced into the metallic wires embedded into the tissues.

Within domain Ω the following equation holds,

$$\nabla \cdot (\sigma \, \nabla\varphi) = i\omega\nabla \cdot (\sigma \, (\boldsymbol{A}_s + \boldsymbol{A}_r)) \,. \tag{4}$$

Eq. (4) is approximated according to the Finite Element Method, using hexahedral elements corresponding to the voxels in which the anatomical human models are discretized. Nodal unknowns are used to represent the scalar potential φ with first order shape functions. Assumption d) leads to the following boundary condition on $\partial\Omega$ for the unknown electric scalar potential,

$$\nabla\varphi \cdot \boldsymbol{n} = i\omega(\boldsymbol{A}_s + \boldsymbol{A}_r) \cdot \boldsymbol{n}, \tag{5}$$

being $\boldsymbol{n}$ the unit vector normal to the boundary $\partial\Omega$.

The metallic filamentary implant is described in terms of 1D curves, which are inserted inside the human body as a separate structure without imposing constraints during the meshing operation. The set of curves is handled as an electrical network, constituted by N nodes and M branches. The curve of a single branch is approximated by a broken line. An unknown current $I_{w,k}$ is associated to the oriented k-th branch of the network, having length d_k and cross section S_k. Under the assumption that the cross section S_k is sufficiently small with respect to the EMF penetration depth in the metal at the frequency under study, the current density $\boldsymbol{J}_{w,k}$ appearing in Eq. (3) is considered uniformly distributed within the cross section and its amplitude is expressed as $I_{w,k}/S_k$.

The fundamental loop currents of the electrical network are identified through a tree/co-tree decomposition and assumed as unknowns. For the j-th fundamental loop $\Im_j$, the following equation holds,

$$\oint_{\Im_j} \sigma^{-1}\boldsymbol{J}_w \cdot dl = -i\omega\oint_{\Im_j} (\boldsymbol{A}_s + \boldsymbol{A}_r) \cdot dl \,. \tag{6}$$

Eq. (6) leads to

$$\sum_{k(j)} R_{k(j)}I_{w,k(j)} = -i\omega\sum_{k(j)} \left(a_{s,k(j)} + a_{r,k(j)}\right), \tag{7}$$

where R_k is the resistance of the k-th branch, $a_{s,k}$ and $a_{r,k}$ denotes the integrals of the magnetic vector potential components (source and reactive ones, respectively) tangential to the k-th branch along the branch itself, and $k(j)$ spans the indices of the branches belonging to the loop $\Im_j$. The currents in all the branches can be collected in a vector $\mathbf{i}_w = \mathbf{C}^T \mathbf{i}_0$, being $\mathbf{C}$ the loop-branch conversion matrix and $\mathbf{i}_0$ the vector of the fundamental loop currents. Eq. (7) can be rewritten using the matrix formalism as:

$$\mathbf{CRC}^T \, \mathbf{i}_0 = -i\omega\mathbf{C}(\mathbf{a}_s + \mathbf{a}_r) \tag{8}$$

being $\mathbf{a}_s$ and $\mathbf{a}_r$ the vectors of elements $a_{s,k}$ and $a_{r,k}$, respectively, and the diagonal matrix $\mathbf{R}$ collects the resistance of each branch.

Since Γ is the union of the M branches, the integral in Eq. (3) can be split in the sum of M line integrals, each one multiplying the current flowing in the corresponding branch. This allows to define $\mathbf{a}_r$ as a linear combination of the branch currents, and consequently of the fundamental loop currents,

$$\mathbf{a}_r = \mathbf{L}\,\mathbf{i}_w = \mathbf{L}\,\mathbf{C}^T \, \mathbf{i}_0, \tag{9}$$

where the inductance matrix $\mathbf{L}$ has been introduced. The evaluation of $\mathbf{L}$ passes through the computation of the line integrals (Eq.

3) along the branches according to an adaptive quadrature rule with a relative tolerance error of 10^{-6}. The diagonal terms of $\mathbf{L}$ exhibit singularity in the Green function and are therefore computed analytically, taking into account the actual wire diameter (see Appendix A).

Finally, the following equation for the fundamental loop currents is obtained by combining Eq. 7, Eq. 8 and Eq. 9,

$$\mathbf{C}(\mathbf{R} + i\omega\mathbf{L})\mathbf{C}^T \, \mathbf{i}_0 = -i\omega\mathbf{C}\,\mathbf{a}_s \tag{10}$$

Once Eq. (10) is solved, the magnetic vector potential due to the currents induced in the metallic wires, $\boldsymbol{A}_r$, can be computed in the biological tissues and brought into the forcing term of Eq. (4). Finally, the power dissipated in each branch of the circuit and that dissipated in the biological tissues are evaluated and used as input for the successive thermal problem.

The electromagnetic formulation described above was implemented in Matlab 2022a [41] and CUDA C [42], adopting GPU acceleration in the computation of the field source.

2.2. Thermal problem

Thermal simulations were carried out in the time domain by solving Pennes' bioheat equation [39] expressed in terms of temperature elevation ΔT with respect to the initial temperature T_0, both disregarding or including thermoregulation processes following the approach proposed in [43].

The heat sources are the power directly deposited within the biological tissues and the contribution coming from the Joule effect in the metallic wires. The latter contribution is modelled by distributing uniformly in each voxel the power associated to the portion of wires which crosses the voxel itself.

The bioheat equation was solved numerically by a finite difference method (FDM) using a Douglas–Gunn (DG) time split scheme also implemented in Matlab 2022a [41] and CUDA C [42]. Details of the numerical implementation can be found in [44].

3. Material and methods

3.1. Verification case study

The validity of the proposed filamentary methodology was verified considering a model problem, consisting in a cylindrical structure, layered along the radius, involving four materials (1–4) and an internal empty compartment (5), mimicking a biliary duct [45,46] (see Fig. 1). This geometry enables a detailed comparison with results provided by FEM simulations in 2D axial-symmetry (see Appendix B for details of this approach), where the mesh can be highly refined. The results of the 2D simulations were assumed as the reference data to verify the accuracy of the proposed approach. Moreover, an additional comparison was also performed using the results provided by the magneto-quasi stationary 3D solver of CST Microwave Studio [47] based on a non-structured mesh of tetrahedra.

The internal and external diameters of the structure are equal to 7 mm and 40 mm, respectively. The axial length is 24 mm. The thickness of the layers 1 to 3 are 0.5 mm. The electrical and thermal properties of the materials are reported in Table 1. For the sake of simplicity, the electrical tissue properties were assumed to be constant with respect to frequency, taking into account that the purpose of the test is a verification of the proposed approach rather than a realistic dosimetric analysis of body tissues.

Six metallic rings, equally distributed along the cylinder axis, are embedded in the structure, intersecting material 1. The diameter of the metallic wire section was chosen equal to 0.1 mm or 0.2 mm. The wires were assumed to be made of nitinol, a Ni-Ti

Table 1

Physical properties of the tissues included in the 2D duct-like structure. For each layer number, the corresponding tissue type in biliary ducts is reported for reference. In the model problem the electrical conductivity was assumed not to vary with frequency (realistic values at 300 kHz were adopted). The tissue permittivity is not reported being disregarded in the proposed approach.

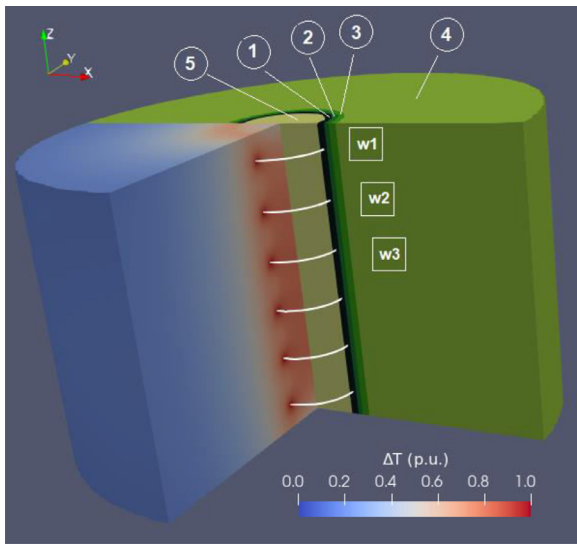| Tissue	1 (mucosa layer)	2 (submucosa layer)	3 (muscularis propria)	4 (connective tissue)
Electrical conductivity (S/m)	0.511	0.251	0.202	0.39
Density (kg/m³)	1088	1027	1090	1027
Heat capacity (J/(kg·K))	3690	2372	3421	2372
Thermal conductivity (W/(m·K))	0.53	0.39	0.49	0.39
Heat transfer rate (ml/(min·kg))	460	37	37	37
Heat generation rate (W/kg)	7.13	0.58	0.91	0.58

Fig. 1. Model problem: duct-like structure with layers 1 to 4, an empty internal part (5) and six metallic wires (w1 to w3 and symmetric). The green color scale identifies the different layers. The colormap shows an example of temperature distribution (in p.u.) determined by the power dissipation in the wires due to the uniform magnetic field oriented along the axis of the structure.

alloy with 1.25 MS/m electrical conductivity often employed in biliary stents, or of Ti-6Al-4 V alloy (0.56 MS/m electrical conductivity) widely used in many prostheses for its excellent corrosion resistance. Two configurations of the metallic rings were considered: #1) each ring is disconnected from the other, #2) the three upper rings are connected together (two in series and one in counter series); the same for the three lower rings. The proposed 3D filamentary approach is applied with a voxel-based discretization of the computational domain with a 0.2 mm voxel size. The circular shape of the rings was approximated by N_s line segments, varying N_s to test its influence on the result accuracy.

A spatially uniform magnetic flux density of 10 mT was applied along the structure axis at a frequency ranging from 10 kHz to 10 MHz. It must be remarked that the characteristics of this model problem enable us to extend the frequency above the limit of normal applicability of the proposed approach. Precisely, the axial-symmetry of the problem guarantees that the induced current density is perpendicular to any longitudinal plane containing the axis of the cylinders. Hence, the currents induced in the loop wires are geometrically confined within the metal, as requested by the assumptions of the filamentary approach. Extending the comparison up to 10 MHz was functional to test the filamentary model under conditions ranging from a feeble to a relevant reaction field, without referring to any specific application.

The electromagnetic solution provided by the proposed approach was verified by comparing the currents induced in the wires, the magnetic flux density amplitude in the center of the domain, and the total power dissipated in the native tissues with those computed by the 2D FEM model and by CST.

Further validations were done on the thermal simulation, to check if the Joule effect in the metallic rings is properly taken into account in the computation of the temperature increase in tissues. The results provided by the 2D FEM model (referred to as FEM2D-p2D) were assumed as the reference, to verify the accuracy of the proposed methodology (referred to as Voxel-3D). Additional results, obtained by imposing the power computed by the proposed electromagnetic solver as forcing term of the 2D FEM thermal model (referred to as FEM2D-p3D), allowed disentangling the errors introduced in the proposed method by the electromagnetic and the thermal solvers.

To make the heating magnitude at different frequencies comparable, before passing the input to the thermal problem, the power losses were rescaled, taking advantage of the linearity of the electromagnetic field problem, to keep the product between B-field amplitude and frequency constant.

3.2. Anatomical head model with orthopedic skull grid

The proposed methodology was applied to the analysis of an anatomical head model carrying an orthopedic skull grid, usually employed for bone repair in case of trauma [48]. The head of the Duke model, belonging to the Virtual Population (ViP) [49,50], was voxelized with a resolution of 1 mm, resulting in ~4.9 10^6 total voxels. The tissue properties were assigned according to the IT'IS database [51], corresponding to the working frequencies of the analyzed technologies.

The considered metallic grid has a size of 55 mm x 55 mm [19]. The planar grid was deformed to fit the surface of the skull, mimicking a real surgery. The grid wires (diameter 0.1 mm or 0.2 mm) are made of ASTM F67 alloy, having electrical conductivity equal to 2.17 MS/m.

The model was exposed to: a) the magnetic field generated by a neck applicator for MH treatment, b) the gradient field of a tubular scanner for MRI, c) the magnetic field generated by a figure-of-eight coil used for TMS. The characteristics of the exposure are considerably different for the three scenarios in terms of frequency, field amplitude, spatial distribution and exposure duration. To the Authors' knowledge, specific data about possible exclusion criteria are currently available mainly for patients bearing implants who should undergo MRI (see for example [52]).

For scenario a), a simplified version of an open collar-type coil, used for the MH treatment of the neck region, was applied [16]. The coil was set to generate a magnetic flux density of 10 mT (peak value) in the central region (target area) in the frequency range from 100 kHz to 300 kHz. The B-field map on the grid is shown in Fig. 2a.

For scenario b), the z-axis coil of a set of realistic gradient coils for tubular MRI scanners (Nanjing Cichen Medical Technology Co., Ltd, Nanjing, China, model SOLARIS) was used. The coil was supplied with a 1 kHz sinusoidal current able to generate a field gradient amplitude of 20 mT/m (peak value) along the axial direction.
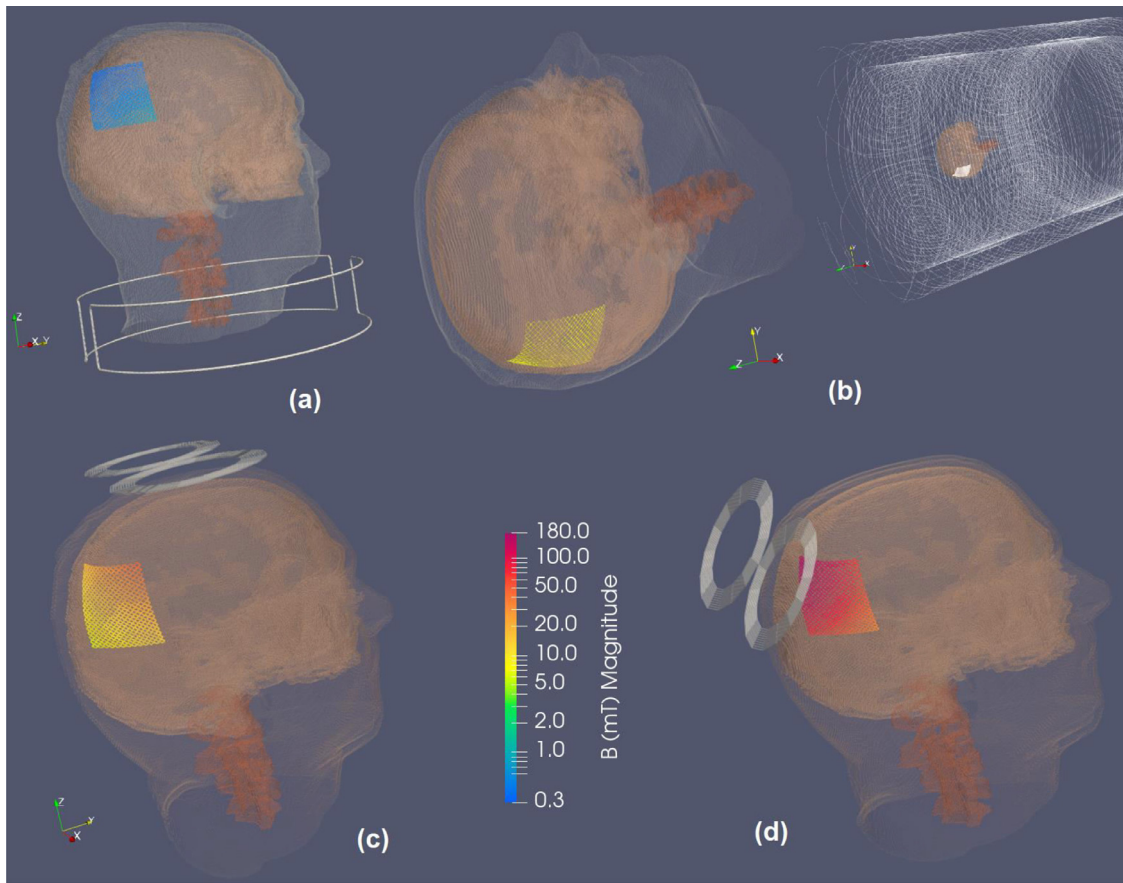
Fig. 2. B-field maps in the implant region produced by the field sources here considered: (a) open collar-type coil used for hyperthermia, (b) system of gradient coils for MRI tubular scanner, (c) and (d) figure-of-eight coil for TMS treatment in two realistic positions.

The head was positioned in the region where the magnetic flux density amplitude was around 7 mT (peak value). The B-field map on the grid is shown in Fig. 2b.

For scenario c), two realistic orientations of the figure-of-eight coil for TMS were analyzed. The coil was supplied at 3 kHz to generate an electric field of amplitude around 150 V/m (peak value) at the brain surface, suitable to perform the stimulation. The corresponding B-field maps on the grid are shown in Fig. 2c and 2d.

4. Results and discussion

4.1. Verification study case

Table 2 reports the currents computed in the rings and the corresponding values of the magnetic flux density in the center of the model structure for configuration #1 (disconnected rings). The results were computed with wire electric conductivity of 0.56 MS/m and diameter of 0.2 mm (Case A), by means of the reference 2D solver, the CST solvers and the proposed simplified approach. The corresponding values of the power dissipated in the tissues are compared in Table 3.

Similar results, but with wire electric conductivity equal to 1.25 MS/m and diameter equal to 0.1 mm (Case B), still for configuration #1 (disconnected rings), can be found in the Supplementary Material Table S.1, comparing the 2D reference solver and the proposed simplified approach.

Table 4 reports the currents computed in the rings and the corresponding values of the magnetic flux density in the center of the structure for configuration #2 (connected rings), both for Case A

Table 2

Results for ring configuration #1: wire thickness equal to 0.2 mm, electric conductivity of the metal equal to 0.56 MS/m. For each case, solutions obtained with three solvers are compared: FEM-2D axial-symmetric (2D), CST using tetrahedra (3D-CST), proposed method (3D-fil). For this latter, results obtained with two values of segments N_s for wire discretization are reported. The B-field comparison is evaluated in the center of the structure.

Quantity	Method	f (kHz)			
		10^1	10^2	10^3	10^4
Current w1 (A)	2D	0.0204	0.204	2.02	14.5
	3D-CST	0.0202	0.203	2.02	14.4
	3D-fil ($N_s = 32$)	0.0202	0.202	2.01	14.2
	3D-fil ($N_s = 16$)	0.0199	0.199	1.98	14.1
Current w2 (A)	2D	0.0207	0.207	2.05	14.2
	3D-CST	0.0206	0.206	2.05	14.1
	3D-fil ($N_s = 32$)	0.0205	0.205	2.04	13.8
	3D-fil ($N_s = 16$)	0.0202	0.202	2.01	13.8
Current w3 (A)	2D	0.0209	0.209	2.07	14.1
	3D-CST	0.0207	0.207	2.06	14.1
	3D-fil ($N_s = 32$)	0.0206	0.206	2.05	13.8
	3D-fil ($N_s = 16$)	0.0203	0.203	2.02	13.8
B-field (mT)	2D	10.0	10.0	9.96	7.52
	3D-CST	10.0	10.0	9.97	7.51
	3D-fil ($N_s = 32$)	10.0	10.0	9.93	7.50
	3D-fil ($N_s = 16$)	10.0	10.0	9.93	7.54

and Case B. In this case, the comparison is limited to the 2D reference solver and the proposed simplified approach.

Plots of the temperature increase reached at steady-state along the radial direction in the mid-section of the cylindrical structure are presented in Fig. 3 (configuration #1) and Fig. 4 (configuration #2), with wire electric conductivity of 0.56 MS/m and diameter of

Table 3

Results for ring configuration #1: wire thickness equal to 0.2 mm, electric conductivity of the metal equal to 0.56 MS/m. For each case, the power dissipated in the tissues obtained with three solvers are compared: FEM-2D axial-symmetric (2D), CST using tetrahedra (3D-CST), proposed method (3D-fil). For this latter, results obtained with two values of segments N_s for wire discretization are reported.

Power (W)	Method	f (kHz)			
		10^1	10^2	10^3	10^4
Tissue 1	2D	$1.7 \ 10^{-3}$	0.171	16.7	811
	3D-CST	$1.7 \ 10^{-3}$	0.170	16.8	813
	3D-fil ($N_s = 32$)	$1.7 \ 10^{-3}$	0.166	16.5	774
	3D-fil ($N_s = 16$)	$1.6 \ 10^{-3}$	0.162	16.0	746
Tissue 2	2D	$7.1 \ 10^{-8}$	$7.1 \ 10^{-6}$	$7.1 \ 10^{-4}$	$4.6 \ 10^{-2}$
	3D-CST	$7.1 \ 10^{-8}$	$7.1 \ 10^{-6}$	$7.0 \ 10^{-4}$	$4.6 \ 10^{-2}$
	3D-fil ($N_s = 32$)	$6.7 \ 10^{-8}$	$6.7 \ 10^{-6}$	$6.7 \ 10^{-4}$	$4.5 \ 10^{-2}$
	3D-fil ($N_s = 16$)	$6.7 \ 10^{-8}$	$6.7 \ 10^{-6}$	$6.7 \ 10^{-4}$	$4.4 \ 10^{-2}$
Tissue 3	2D	$7.9 \ 10^{-8}$	$7.9 \ 10^{-6}$	$7.9 \ 10^{-4}$	$5.7 \ 10^{-2}$
	3D-CST	$7.9 \ 10^{-8}$	$7.9 \ 10^{-6}$	$7.9 \ 10^{-4}$	$5.7 \ 10^{-2}$
	3D-fil ($N_s = 32$)	$8.7 \ 10^{-8}$	$8.7 \ 10^{-6}$	$8.6 \ 10^{-4}$	$6.2 \ 10^{-2}$
	3D-fil ($N_s = 16$)	$8.7 \ 10^{-8}$	$8.7 \ 10^{-6}$	$8.6 \ 10^{-4}$	$6.3 \ 10^{-2}$

Table 4

Results for ring configuration #2. Case A (wire thickness equal to 0.2 mm, electric conductivity of the metal equal to 0.56 MS/m) and Case B (wire thickness equal to 0.1 mm, electric conductivity of the metal equal to 1.25 MS/m). Variable number of segments N_s for wire discretization. The B-field comparison is evaluated in the center of the structure.

| Case	Quantity	Method	f (kHz)			
			10^1	10^2	10^3	10^4
A	Current w1/w2/w3 (A)	2D	0.00680	0.0681	0.676	5.30
		3D-fil ($N_s = 32$)	0.00680	0.0677	0.675	5.28
		3D-fil ($N_s = 16$)	0.00670	0.0668	0.667	5.26
	B-field (mT)	2D	10.0	10.0	9.99	9.35
		3D-fil ($N_s = 32$)	10.0	10.0	9.99	9.37
		3D-fil ($N_s = 16$)	10.0	10.0	9.99	9.38
B	Current w1/w2/w3 (A)	2D	0.00380	0.0382	0.381	3.36
		3D-fil ($N_s = 32$)	0.00380	0.0378	0.377	3.32
		3D-fil ($N_s = 16$)	0.00380	0.0373	0.377	3.29
	B-field (mT)	2D	10.0	10.0	9.97	9.35
		3D-fil ($N_s = 32$)	10.0	10.0	10.0	9.69
		3D-fil ($N_s = 16$)	10.0	10.0	10.0	9.69
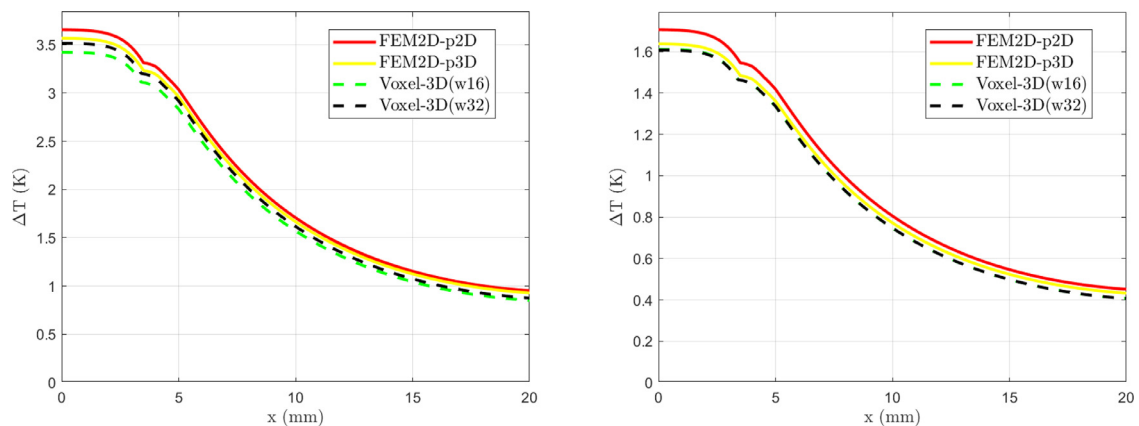
Fig. 3. Ring configuration #1 with wire thickness equal to 0.2 mm and electric conductivity of the metal equal to 0.56 MS/m. Variable number of segments N_s for wire discretization (w16 and w32 in the legend). Temperature increase along the radial direction. On the left results at 100 kHz, on the right results at 10 MHz.

0.2 mm (see Supplementary Material Fig. S.1 and S.2 for the results with wire electric conductivity of 1.25 MS/m and diameter of 0.1 mm).

The results evidence a good agreement of the proposed filamentary approach (3D-fil in the tables) with the 2D and the CST solvers, evaluated in quantitative terms for the phenomena induced both within the metallic wires and in the surrounding tissues. The effects of the reaction field increase the error with the frequency, because of numerical inaccuracies in computing the reaction field near to the wires. The error is also slightly affected by the number of segment N_s used to discretize the wire. The error in the current amplitude was always lower than 3% with respect to the 2D solution. Such a result translates in an error of ~5% on the estimate of the power dissipated within the wires and ~10% on the estimated power in tissues. The latter error, however, is not due to the proposed approach, but to the adoption of a voxel-based structured mesh to discretise the computational domain.

The results of the proposed filamentary approach are obtained with ~3.7 10^6 voxels and the computations time for each single solution is ~14 min, running on a Intel Xeon Gold 6238R processor and NVIDIA A100 GPU accelerator. As a comparison, the commercial software CST working on a mesh with ~0.79 10^6 tetrahedra required ~21 min running on an Intel Xeon CPU E5–2650 v3 processor and NVIDIA Quadro K6000 GPU accelerator.
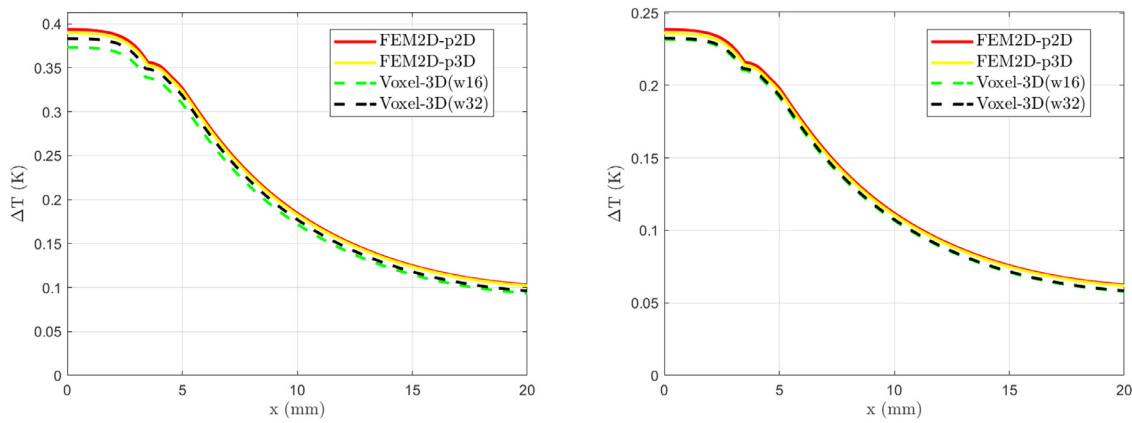
Fig. 4. Ring configuration #2 with wire thickness equal to 0.2 mm and electric conductivity of the metal equal to 0.56 MS/m. Variable number of segments N_s for wire discretization (w16 and w32 in the legend). Temperature increase at steady-state along the radial direction. On the left results at 100 kHz, on the right results at 10 MHz.
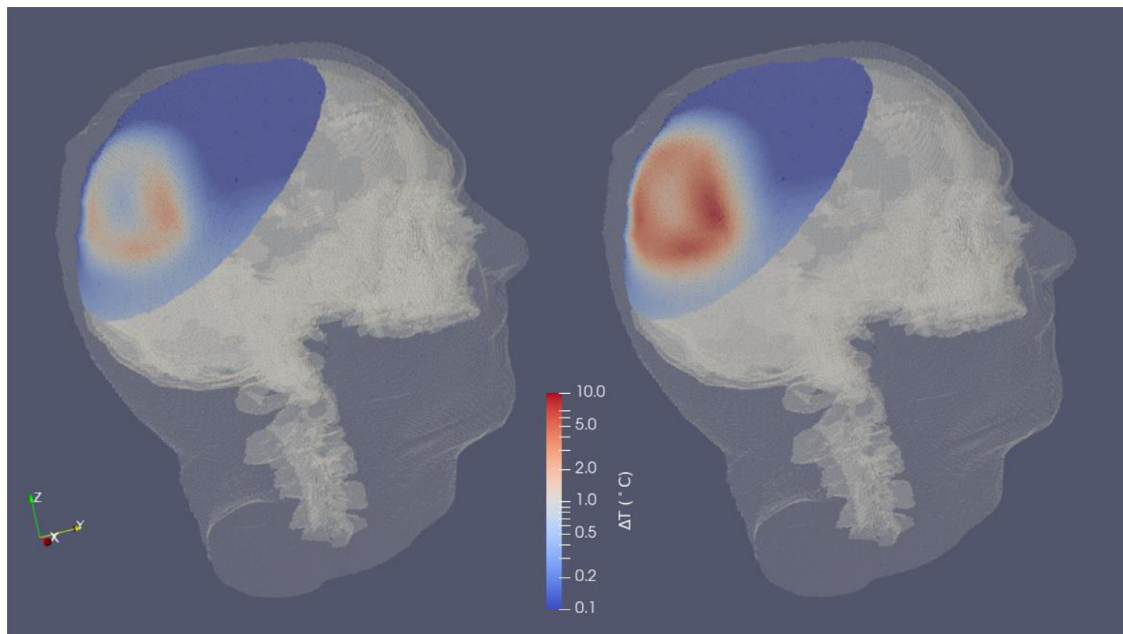

Fig. 5. Spatial distribution of the temperature increase (ΔT) after 1800s in tissues close to the orthopedic grid for a B-field value in the target area equal to 10 mT at 300 kHz. The wire diameter is equal to 0.1 mm (left plot) and 0.2 mm (right plot). The results shown here were obtained in absence of thermoregulation.

Regarding the testing on thermal solutions, an error of ~5% in the temperature increase in tissues suggests that the approximation adopted when distributing the dissipated power within the voxels is adequate to the purpose, because the error is kept in the same order of magnitude as in the computed Joule losses in the wires. Moreover, it means that the power directly deposited in the tissues, where the error due to the voxel structure is larger, is negligible with respect to the Joule losses in the wires. Figs. 3 and 4 show also that the temperature trends estimated by FEM2D-p3D and Voxel-3D are consistent, providing further confirmation of the previous analysis.

4.2. Anatomical head model with orthopedic skull grid

4.2.1. Magnetic hyperthermia

The field is applied continuously for 30 min, as in a realistic MH treatment. Simulations have been performed both with and without the thermoregulation effects. The computation time is ~20 min for the electromagnetic solver and ~1.4 s for each time step of the transient thermal solver; all these data refer to a run on an Intel Xeon Gold 6238R processor and NVIDIA A100 GPU accelerator.

The maximum temperature increases reached in close proximity of the grid are listed in Table 5. At 300 kHz, the values range from 2.5 °C to 10.0 °C depending on the wire size and the presence/absence of thermoregulation. Decreasing the supply frequency to 100 kHz, the temperature increase reduces to 1.2 °C for the wire diameter of 0.2 mm. Fig. 5 shows the spatial distribution of the temperature increases at 300 kHz in proximity of the metallic grid, without thermoregulation, for grids having wire diameters of 0.1 mm and 0.2 mm.

The results put in evidence a localized heating in proximity of the implant, which is affected by the grid geometrical characteristics. The non-negligible thermal effects evidence the usefulness of the proposed tool of analysis for evaluating potential exclusion criteria for patients carrying this type of implant.

4.2.2. MRI gradient coils

The field is applied continuously for 30 min, simulating a continuous MRI acquisition session. The computation time is ~11 min for the electromagnetic solver and ~1.4 s for each time step of the thermal solver; all these data refer to a run on an Intel Xeon Gold 6238R processor and NVIDIA A100 GPU accelerator.

Table 5

Maximum temperature increase (ΔT) with and without thermoregulation after 1800s in tissues close to the orthopedic grid for different diameter of the grid and supply frequency. B-field value in the target area equal to 10 mT.

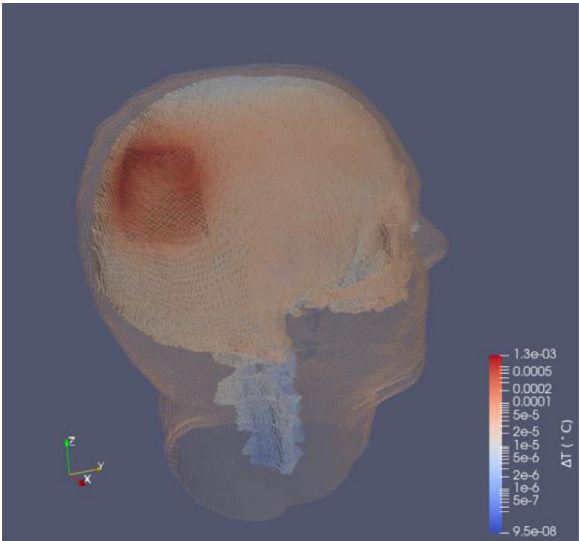| Frequency (kHz)	Wire diameter (mm)	Max ΔT (°C)	
		With thermoregulation	Without thermoregulation
300	0.1	2.5	6.9
300	0.2	2.8	10.0
100	0.2	1.2	1.2

Fig. 6. Spatial distribution of the temperature increase after 1800s. The temperature increase due to the grid is almost negligible.

The temperature increase in proximity of the metallic grid after 30 min is negligible, considerably below 0.001 °C (see Fig. 6). The thermal effect produced by the gradient fields of the scanner on this implant and for this specific case of exposure suggests that, from the point of view of the heating driven by gradient fields, the exam is safe. Of course, this consideration is not general for exposure of these implants to MRI gradient fields and will depend on the specific exposure scenario (type of gradient coils, MRI sequence, implant characteristics).

4.2.3. TMS treatment

Due to the short duration of the field application (which limits the thermal effects), the simulations were focused on the modifications in the spatial distribution of the induced electric field in the brain tissues produced by the metallic orthopedic grid placed in proximity of the region of treatment (see Fig. 2c and 2d). For both the coil positions, it was observed that the grid does not modify neither the spatial pattern, nor the amplitude of the induced electric field. An example of the spatial distribution of the electric field in the brain tissue is reported in Fig. 7, comparing the spatial distribution with and without the grid. The computations time is ~15 min for the electromagnetic solver running on an Intel Xeon Gold 6238R processor and NVIDIA A100 GPU accelerator.
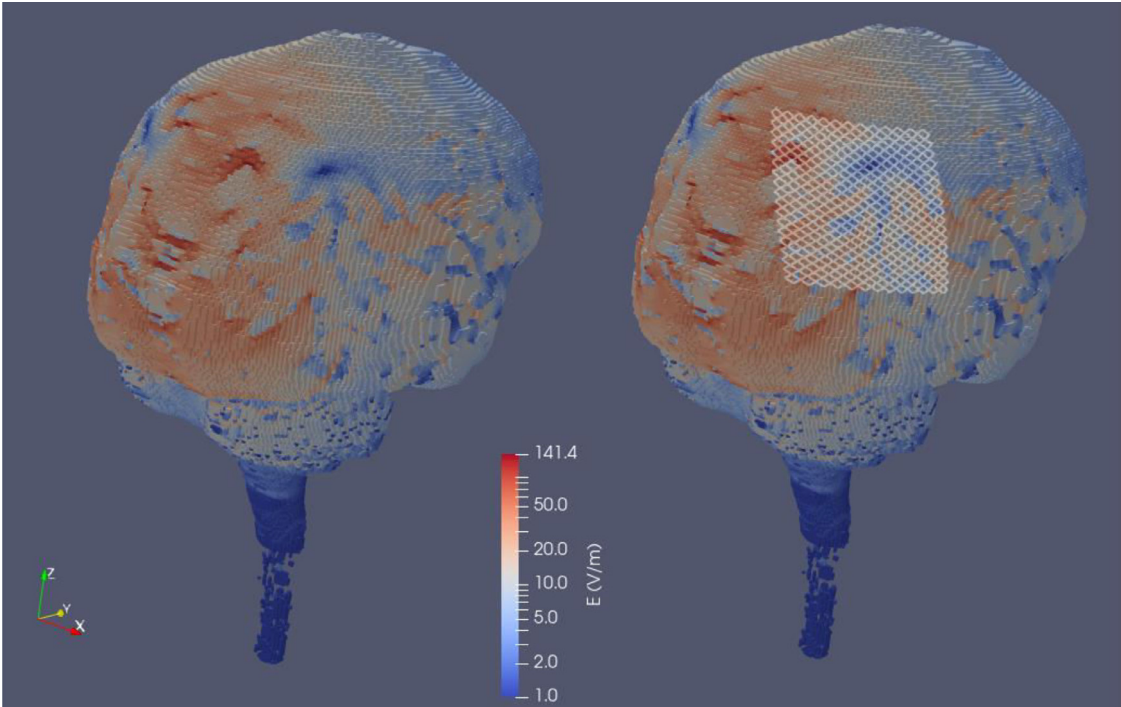

Fig. 7. Spatial distribution of the amplitude of the induced electric field (E) in the gray matter, white matter, cerebellum and cerebrospinal fluid in absence (left) or in presence (right) of the grid. The effect of the grid on the E-field is almost negligible.

5. Conclusions

A simplified approach was developed specifically to handle the presence of looped metallic wire implants within anatomical human models. Despite the approximations introduced in the procedure, a good accuracy was found by comparing the results on a test model with a 2D axisymmetric FEM solver (used as a reference) and a 3D commercial software (average errors in current amplitudes induced in the wires around 2.5% up to 1 MHz, which results in errors lower than 5% in terms of power released in the metallic components and 10% in power density in tissues). At the same time, comparable or even better computational time is found with respect to the considered commercial software making reference to the test problem.

The proposed tool was also found to be easily applicable in realistic exposure scenario analysis, since it requires only a description of the metallic implant as a 1D geometrical object, independently of the adopted human body discretization. Similar analysis adopting a standard approach will require embedding the filamentary wire into the discretization of the body tissues, being demanding from the pre-processing step and affecting the total computational time of the solver.

Of course, the filamentary approach proposed here has some limitations that must be taken into account when dealing with the analysis of realistic exposure of patients carrying implants. In particular, propagation effects are not taken into account with this approach; this limits the application to frequencies below about 1 MHz for human bodies.

Moreover, the currents induced in the filamentary wires should be confined within the metallic parts. This feature limits the application of the filamentary approach to passive implants with closed loops, precluding its use for open wires as electrodes of cardiac and brain stimulators. As a consequence, the applicability of the proposed approach has to be evaluated case by case depending on the characteristics of the studied implant. Despite these limitations, the proposed tool is tailored to a detailed analysis of different types of small implants, ranging from coronary and biliary duct stents to orthopedic grids in a large variety of exposure scenarios.

Declaration of Competing Interest

All Authors declare that they have no conflict of interest.

Acknowledgements

Supplementary materials

Supplementary material associated with this article can be found, in the online version, at doi:10.1016/j.cmpb.2022.107316.

Appendix A

To overcome the singularity in the Green function in the computation of the diagonal terms of inductance matrix $\mathbf{L}$, an analytical equation is adopted. Considering one of the elementary segments in which the generic k-th branch is discretized, having cylindrical shape of length L and section area πR^2, it is assumed that the current (unitary amplitude) is confined in the cylindrical axis and the line integral of the vector potential A_r is substituted by the volume integral over the entire cylindrical domain (volume V):

$$\int_L A_r \, ds = \frac{1}{\pi R^2} \int_V A_r \, dv = \frac{1}{\pi R^2} 2\pi \int_0^R \left(\int_0^L A_r(r,y) dy \right) r dr \quad (A.1)$$

In (A.1) the rotational symmetry of the domain and the vector potential are exploited. This volume integral is convergent and lead to the following expression:

$$\int_V A_r \, dv = \frac{2\pi}{3}$$

$$\times \left[\sqrt{L^2 + R^2} \left(L^2 - 2R^2 \right) + \left(2R^3 - L^3 \right) + 3LR^2 \log \left(\frac{\sqrt{L^2 + R^2} + L}{R} \right) \right]$$

$$(A.2)$$

Appendix B

The 2D axialsymmetric solver used to have a reference solution in the electromagnetic testing is based on a $\mathbf{A}$-φ formulation in the frequency domain. The code, specific for voltage driven problems, simultaneously solves the field equation, which includes unknown currents, and the electric network equations, where the induced electromotive forces are expressed in terms of the unknown magnetic vector potential $\mathbf{A}$.

The weak form of the field equation, written in the frequency domain (angular frequency ω), is:

$$\int_\Omega \nu \, \text{curl} \, \mathbf{A} \cdot \text{curl} \, \mathbf{w} \, ds$$

$$= \sum_k \left[\int_{\Omega_k} \frac{\mathbf{i}_k}{S_k} \cdot \mathbf{w} \, ds - \mathrm{i}\omega\sigma_k \int_{\Omega_k} \mathbf{A} \cdot \mathbf{w} \, ds + \mathrm{i}\omega\sigma_k \int_{\Omega_k} M_k(\mathbf{A}) \cdot \mathbf{w} ds \right]$$

$$(B.1)$$

where i is the imaginary unit, ν the local magnetic absolute reluctivity, $\mathbf{w}$ is the test function, Ω is the entire geometrical domain under study, k indicates a generic conductor or coil having trace Ω_k, area S_k and current i_k (whose spatial orientation is identical to vector $\mathbf{A}$). The mean of $\mathbf{A}$ over Ω_k is expressed by

$$M_k(\mathbf{A}) = \frac{\int_{\Omega_k} \mathbf{A} ds}{r \int_{\Omega_k} \frac{1}{r} ds} \quad (B.2)$$

Eq. (B.1) is discretized using the finite element method. Linear shape functions are employed in a region around the symmetry axis, while elsewhere the same shape functions are weighted by r^{-1}. This approach, requiring the imposition of internal continuity conditions, is allowed by the facilities of the mesh generator included in the computational package developed by some of the Authors.

Unknown currents i_k appearing in Eq. (B.1) and involving external circuits are computed coupling the discretized field equation with the circuital equations, where the electromotive forces are linked to the values of vector potential $\mathbf{A}$. More details can be found in [53].

References

[1] Vijay Prakash Mathur, Mohammad Atif, Isha Duggal, Nitesh Tewari, Ritu Duggal, Anoop Chawla, Reporting guidelines for in-silico studies using finite element analysis in medicine (RIFEM), Comput. Methods Programs Biomed. 216 (2022) 106675.

[2] https://www.alliedmarketresearch.com/implantable-medical-devices-market. Accessed on-line on June 3rd, 2022.

[3] Roy Beinart, Saman Nazarian, Effects of external electrical and magnetic fields on pacemakers and defibrillators: from engineering principles to clinical practice, Circulation 128 (25) (2013) 2799–2809.

[4] Qi Zeng, Qinyan Wang, Jianfeng Zheng, Wolfgang Kainz, Ji Chen, Evaluation of MRI RF electromagnetic field induced heating near leads of cochlear implants, Phys. Med. Biol. 63 (13) (2018) 135020.

[5] Luca Santini, Giovanni B. Forleo, Massimo Santini, Implantable devices in the electromagnetic environment, J. Arrhythm. 29 (6) (2013) 325–333.

[6] Ran Guo, Jianfeng Zheng, Ji Chen, MRI RF-Induced heating in heterogeneous human body with implantable medical device, in: Ahmet Mesrur Halefoğlu (Ed.), High-Resolution Neuroimaging, Basic Physical Principles and Clinical Applications, 2017.

[7] Katsumi Kose, Physical and technical aspects of human magnetic resonance imaging: present status and 50 years historical review, Adv. Phys. 6 (1) (2021) 1885310.

[8] A. Rajan, N.K. Sahu, Review on magnetic nanoparticle-mediated hyperthermia for cancer therapy, J. Nanopart. Res. 22 (2020) 319.

[9] A. Chail, R.K. Saini, P.S. Bhat, K. Srivastava, V. Chauhan, Transcranial magnetic stimulation: a review of its evolution and current applications, Ind. Psychiatry J. 27 (2) (2018) 172–180.

[10] Johannes B Erhardt, Erwin Fuhrer, Oliver G Gruschke, Jochen Leupold, Matthias C Wapler, Jürgen Hennig, Thomas Stieglitz, Jan G Korvink, Should patients with brain implants undergo MRI? J. Neural Eng. 15 (2018) 041002.

[11] Bobby Kalb, Julia H. Indik, Peter Ott, Diego R. Martin, MRI of patients with implanted cardiac devices, J. Magn. Reson. Imaging 47 (2018) 595–603.

[12] Lukas Winter, Frank Seifert, Luca Zilberti, Manuel Murbach, Bernd Ittermann, MRI-Related heating of implants and devices: a review, J. Magn. Reson. Imaging 53 (2020) 1646–1665.

[13] John Powell, Annie Papadaki, Jeff Hand, Alister Hart, Donald McRobbie, Numerical simulation of SAR induced around Co-Cr-Mo hip prostheses in situ exposed to RF fields associated with 1.5 and 3 T MRI body coils, Magn. Reson. Med. 68 (2012) 960–968.

[14] Ting Song, Zhiheng Xu, Maria Ida Iacono, Leonardo M. Angelone, Sunder Rajan, Retrospective analysis of RF heating measurements of passive medical implants, Magn. Reson. Med. 80 (6) (2018) 2726–2730.

[15] A. Arduino, O. Bottauscio, R. Brühl, M. Chiampi, L. Zilberti, In silico evaluation of the thermal stress induced by MRI switched gradient fields in patients with metallic hip implant, Phys. Med. Biol. 64 (2019) 245006.

[16] I. Rubia-Rodríguez, L. Zilberti, A. Arduino, O. Bottauscio, M. Chiampi, D. Ortega, In silico assessment of collateral eddy current heating in biocompatible implants subjected to magnetic hyperthermia treatments, Int. J. Hyperthermia 38 (1) (2021) 846–861.

[17] Riccardo Torchio, Alessandro Arduino, Luca Zilberti, Oriano Bottauscio, A fast tool for the parametric analysis of human body exposed to LF electromagnetic fields in biomedical applications, Comput. Methods Programs Biomed. 214 (2022) 106543.

[18] J.M. Dumonceau, D. Heresbach, J. Deviere, G. Costamagna, U. Beilenhoff, A. Riphaus, et al., Biliary stents: models and methods for endoscopic stenting, Endoscopy 43 (7) (2011) 617–626.

[19] https://www.medartis.com/en-us/products/detail/modusr-mesh/. Accessed online on June 3rd, 2022.

[20] Laleh Golestanirad, Leonardo M. Angelone, Maria Ida Iacono, Husam Katnani, Lawrence L. Wald, Giorgio Bonmassar, Local SAR near Deep Brain Stimulation (DBS) electrodes at 64 and 127 MHz: a simulation study of the effect of extracranial loops, Magn. Reson. Med. 78 (2017) 1558–1565.

[21] Laleh Golestanirad, et al., Changes in the specific absorption rate (SAR) of radiofrequency energy in patients with retained cardiac leads during MRI at 1.5T and 3T, Magn. Reson. Med. 81 (2019) 653–669.

[22] K.R. Umashankar, A. Taflove, A novel method to analyze electromagnetic scattering of complex objects, IEEE Trans. Electromagn. Compatibil., 24 (4): 397–405.

[23] E. Cabot, T. Lloyd, A. Christ, W. Kainz, M. Douglas, G. Stenzel, S. Wedan, N. Kuster, Evaluation of the RF heating of a generic deep brain stimulator exposed in 1.5 T magnetic resonance scanners, Bioelectromagnetics 34 (2013) 104–113.

[24] S. Feng, R. Qiang, W. Kainz, J. Chen, A technique to evaluate MRI-induced electric fields at the ends of practical implanted lead, IEEE Trans Microw Theory Tech 63 (2015) 305–313.

[25] Youngdae Cho, Hyoungsuk Yoo, RF Heating of implants in mri: electromagnetic analysis and solutions, iMRI 24 (2020) 67–75.

[26] Bastien Guerin, et al., Realistic modeling of deep brain stimulation implants for electromagnetic MRI safety studies, Phys. Med. Biol. 63 (2018) 095015.

[27] Maria Ida Iacono, Nikos Makris, Luca Mainardi, Leonardo M. Angelone, Giorgio Bonmassar, MRI-Based multiscale model for electromagnetic analysis in the human head with implanted DBS, Comput Math Methods Med (2013) 694171.

[28] Peter R.S. Stijnman, Bart R. Steensma, Cornelis A.T. van den Berg1, Alexander J.E. Raaijmakers, A perturbation approach for ultrafast calculation of RF field enhancements near medical implants in MRI, Sci. Rep. 12 (2022) 4224.

[29] Davide Santoro, Lukas Winter, Alexander Muller, Julia Vogt, Wolfgang Renz, Celal Ozerdem, Andreas Grassl, Valeriy Tkachenko, Jeanette Schulz-Menger, Thoralf Niendorf, Detailing radio frequency heating induced by coronary stents: a 7.0 tesla magnetic resonance study, PLoS One 7 (11) (2012) e49963.

[30] Swen Großmann, Robert Ott, Richard Kosub, Wolfram Schmidt, Niels Grabow, Klaus-Peter Schmitz, Stefan Siewert, Numerical investigation of stent designs for wireless access to integrated sensors, Curr. Direct. Biomed. Eng. 5 (1) (2019) 497–500.

[31] L. Zilberti, U. Zanovello, A. Arduino, O. Bottauscio, M. Chiampi, RF-induced heating of metallic implants simulated as PEC: is there something missing? Magn. Reson. Med. 85 (2021) 583–586.

[32] S.M. Park, R. Kamondetdacha, J.A. Nyenhuis, Calculation of MRI-induced heating of an implanted medical lead wire with an electric field transfer function, J. Magn. Reson. Imaging 26 (2007) 1278–1285.

[33] J.P. Tokaya, A.J.E. Raaijmakers, P.R. Luijten, J.F. Bakker, C.A.T. van den Berg, MRI-Based transfer function determination for the assessment of implant safety, Magn. Reson. Med. 78 (2017) 2449–2459.

[34] Kyoko Fujimoto, Leonardo M. Angelone, Elena Lucano, Sunder S. Rajan, Maria Ida Iacono, Radio-frequency safety assessment of stents in blood vessels during magnetic resonance imaging, Front Physiol 9 (2018) 1439.

[35] Ilaria Liorni, Esra Neufeld, Manuel Murbach SvenKühn, Earl Zastrow, Wolfgang Kainz, Niels Kuster, Novel mechanistic model and computational approximation for electromagnetic safety evaluations of electrically short implants, Phys. Med. Biol. 63 (2018) 225015.

[36] Janot P. Tokaya, Alexander J.E. Raaijmakers, Peter R. Luijten, Alessandro Sbrizzi, Cornelis A.T. van den Berg, MRI-based transfer function determination through the transfer matrix by jointly fitting the incident and scattered $B+1$ field, Magn. Reson. Med. 83 (2020) 1081–1095.

[37] P. Syrek, M. Skowron, The impact of overhead lines for employees with stents, innovative ideas in science 2016, IOP Conf. Ser. 200 (2017) 012013.

[38] Cristian Barza, Marek Pettersb, Adam Dorszb, Przemysław Syrekb, Possible interactions between stent and electromagnetic field, Sci, Tech. Innov. 3 (2) (2018) 48–51.

[39] H.H. Pennes, Analysis of tissue and arterial blood temperatures in the resting human forearm, J. Appl. Physiol. 1 (1948) 93–122.

[40] Eugene H. Wissler, Pennes' 1948 paper revisited, J. Appl. Physiol. 85 (1) (1998) 35–41.

[41] MATLAB, Mathworks, https://ch.mathworks.com/products/matlab.html?s_tid=hp_ff_p_matlab.

[42] CUDA Toolkit 2022. [ONLINE]. Available: https://developer.nvidia.com/cuda-toolkit.

[43] I. Laakso, A. Hirata, Dominant factors affecting temperature rise in simulations of human thermoregulation during RF exposure, Phys. Med. Biol. 56 (2011) 7449–7471.

[44] A. Arduino, O. Bottauscio, M. Chiampi, L. Zilberti, Douglas–Gunn method applied to dosimetric assessment in magnetic resonance imaging, IEEE Trans. Magn. 53 (2017) 1–4, doi:10.1109/TMAG.2017.2658021.

[45] M. Strazzabosco, L. Fabris, Functional anatomy of normal bile ducts, Anat. Rec. 291 (6) (2008) 653–660.

[46] C. Bonsignore, Open stent design, NDC 47533 (2011) 20–47.

[47] CST Microwave Studio. https://www.3ds.com/products-services/simulia/products/cst-studio-suite/solvers/.

[48] S.T. Chen, C.J. Chang, W.C. Su, L.W. Chang, I.H. Chu, M.S. Lin, 3-D titanium mesh reconstruction of defective skull after frontal craniectomy in traumatic brain injury, Injury 46 (1) (2015) 80–85.

[49] Marie-Christine Gosselin, Esra Neufeld, Heidi Moser, Eveline Huber, Silvia Farcito, Livia Gerber, Maria Jedensjo, Isabel Hilber, Fabienne Di Gennaro, Bryn Lloyd, Emilio Cherubini, Dominik Szczerba, Wolfgang Kainz, Niels Kuster, Development of a new generation of high-resolution anatomical models for medical device evaluation: the virtual population 3.0, Phys. Med. Biol. 59 (18) (2014) 5287–5303.

[50] Sim4Life, Computable human phantoms, Zurich MedTech AG, Zurich https://zmt.swiss/sim4life/. Accessed online on Jun. 3rd 2022.

[51] P.A. Hasgall, F. Di Gennaro, C. Baumgartner, E. Neufeld, B. Lloyd, M.C. Gosselin, D. Payne, A. Klingenböck, N. Kuster, It'is Database for Thermal and Electromagnetic Parameters of Biological Tissues, Version 4.0, 2018 May 15Itis.swiss/database, doi:10.13099/VIP21000-04-0.

[52] https://www.mrisafety.com/. Accessed online on Jun. 16th 2022.

[53] O. Bottauscio, M. Chiampi, A. Manzin, Diffusion and hysteresis in axisymmetric electromechanical devices, IEEE Trans. Mag. 39 (2) (2003) 990–997.